

Determining Turbulent Kinetic Energy Dissipation from Batchelor Curve Fitting

DAVID A. LUKETINA¹

AND

JÖRG IMBERGER²

¹SCHOOL OF CIVIL AND ENVIRONMENTAL ENGINEERING

UNIVERSITY OF NEW SOUTH WALES

²CENTRE FOR WATER RESEARCH

UNIVERSITY OF WESTERN AUSTRALIA

Submitted to the Journal of Atmospheric and Oceanic Technology

23 November 1998

Water Research Laboratory Report WRL 198

Centre for Water Research Report ED 648 DL

Corresponding Author:

Dr David Luketina, email: d.luketina@unsw.edu.au

Water Research Laboratory, University of New South Wales, King St, Manly Vale, NSW 2093. AUSTRALIA.

ABSTRACT

A robust algorithm is presented for obtaining the rate of turbulent kinetic energy dissipation by fitting the theoretical Batchelor spectrum to the temperature gradient spectrum at high wavenumbers. The algorithm is successful in selecting the turbulent Batchelor component from temperature gradient spectra, which have finestructure, internal wave and noise contributions. The theoretical curve is fitted using an error function that takes into account many of the characteristics of the Batchelor spectrum. Overall, the use of the algorithm to determine dissipation of the turbulent kinetic energy, results in considerable time savings when compared to manual methods. The accuracy of the method is also discussed.

1 Introduction

The rate of turbulent kinetic energy dissipation ε is an important parameter in turbulent mixing theory. Knowledge of the magnitude of ε allows the estimation of the rate of vertical mixing (Gregg *et al.* 1977a; Ivey and Imberger, 1991; and Saggio and Imberger, 1999).

It is well known that the higher wavenumber part of the one-dimensional temperature gradient spectrum due to turbulence (the Batchelor spectrum) is a function of the dissipation ε and the dissipation of temperature variance χ_T . Stewart and Grant (1962) describe a graphical method for fitting a non-dimensionalised Batchelor spectrum to temperature gradient data to obtain the dissipation ε . Dillon and Caldwell (1980) and Dillon (1982) used a non-linear least squares method to fit the Batchelor spectrum to well resolved temperature gradient spectra with high signal to noise levels. Some temperature gradient spectra are difficult to fit in this way because of instrument noise at the high wavenumber end of the spectra (Gregg *et al.* 1986), internal wave and finestructure ‘contamination’ at the low wavenumber end of the spectra (Gregg 1977a, b), and the lack of a clearly defined viscous-

convective subrange (Sherman and Davis, 1995). Fig. 1 depicts typical spectra with these additional spectral components.

In this paper, we present an algorithm for obtaining ε by fitting the theoretical Batchelor spectrum to the measured spectrum. Key issues in fitting the theoretical Batchelor curve which are discussed in this paper are: 1) what is the appropriate portion of the measured spectrum to use, 2) how should the dissipation of temperature variance χ_T be determined from the measured spectrum, and 3) what is an appropriate error function to use in determining the optimum fit? The fitting algorithm has been developed and refined over a period of several years and has been successfully applied to temperature gradient spectra from a wide variety of turbulent forcing in the field (eg Luketina and Imberger, 1989; Imberger and Ivey 1991; and Saggio and Imberger, 1999) and in the laboratory (eg Teoh et al, 1997; and De Silva et al, 1997). The data discussed in this paper were generally collected at 100 Hz using an FP07 thermistor mounted on a probe rising or falling at a nominal velocity of 0.1 m s^{-1} . However, the algorithm can be applied to a probe travelling in any direction and at velocities other than of 0.1 m s^{-1} .

The paper is divided into six sections. In Section 2 the features of temperature gradient spectra are discussed. Data requirements, including pre-processing of data, are covered in section 3. The method for obtaining the dissipation ε by fitting the theoretical Batchelor spectrum to the measured temperature gradient spectrum (hereafter referred to as the measured spectrum) is outlined in Section 4. Results from the application of the fitting method to measured and artificially generated spectra are discussed in section 5. Conclusions are presented in section 6.

2. Temperature Gradient Spectra

The typical temperature gradient spectrum shown in Fig. 1 has five different components as shown. These components are due to finestructure, internal waves, inertial-convective turbulence (the inertial-convective subrange), turbulence affected by viscosity and diffusivity (the Batchelor spectrum) and noise.

Finestructure

The most commonly observed finestructure occurs when a probe passes vertically through a stationary thermally stratified fluid. This results in a spectrum with a negative slope, which is quantified as follows: the vertical temperature profile in many regions of a stable temperature stratified fluid can be represented by

$$T = T_0 + \beta |z'|^\gamma \text{sgn } z', \quad \gamma > 0, \beta > 0 \quad (1)$$

where γ and β are constants, z' is the vertical ordinate whose origin is at the centre of the region of interest and is positive upwards, and T_0 is the temperature at the centre of the region. The temperature gradient is thus given by

$$\frac{dT}{dz'} = \gamma \beta |z'|^{\gamma-1} \text{sgn } z'. \quad \gamma > 0, \beta > 0 \quad (2)$$

Examples of stable 1 m long temperature profiles with a 1 °C change from top to bottom, which satisfy (1), are shown in Fig. 2a. By examining Fig. 2a it is clear that (2) describes a wide range of stable temperature profiles. In practice, it is expected that γ would most likely be in the range $0 < \gamma < 2$ (β then depends on the temperature change from the top to the bottom of the profile).

The one-sided finestructure power spectrum $S_f(k)$ of (2) is given by $S_f(k) = 2F(k)F^*(k)$, where F denotes the Fourier transform of dT/dz' and the asterisk denotes the complex conjugate and k is the wavenumber in rad m^{-1} . The Fourier transform of (2) is (Lighthill 1958 pg 43)

$$F(k) = 2\gamma\beta \cos\left(\frac{\gamma\pi}{2}\right) \Gamma(\gamma) (2\pi|k|)^{-\gamma}, \quad \gamma > 0, \beta > 0 \quad (3)$$

where $\Gamma(\gamma+1) = \int_0^\infty x^\gamma e^{-x} dx$. Thus $S_f(k)$ is given by

$$S_f(k) = c_f k^{-2\gamma}, \quad \gamma > 0 \quad (4)$$

where $c_f = 8[(2\pi)^{-\gamma} \gamma\beta \cos(\gamma\pi/2) \Gamma(\gamma)]^2$. For γ in the expected range of $0 < \gamma < 2$ the slope of the spectrum, as given by (4), will be between 0 and -4 in log-log space.

Band averaged spectra $S_f(k)$ of the gradients of the temperature profiles of Fig. 2a are shown in Fig. 2b. The temperature gradients were determined by applying a Gaussian gradient filter to the temperature profiles - this removed the problem of the temperature gradient as given by (2) becoming infinite at $z' = 0$. The temperature gradient data record was then windowed (see Press *et al.* 1989 pg 423 for details) prior to applying a discrete Fourier transform to yield $F(k)$. The filtering is responsible for the spectra with $\gamma = 0$ and $\gamma = 0.5$ deviating from the theoretical spectra given by (4) at wavenumbers above approximately 300 cpm . The spectrum with $\gamma = 2$ deviates because the high frequency content of the temperature gradient profile is located at the ends of the data record which are subsequently modified by windowing. In any case, it is expected that the finestructure spectrum $S_f(k)$ derived via discrete Fourier transforms will generally have a slope of between 0 and -4 at low wavenumbers in log-log space.

Internal Waves

Internal waves with a wavelength smaller than the Rossby radius (Pedlosky 1987, pg 9) will have a temperature gradient spectrum of the form (Gregg *et al.* 1991)

$$S_w(k) = c_w \left(\frac{dT}{dz} \right)^2 k^{-1}, \quad (5)$$

where the subscript w denotes internal waves and, based on the data of Gregg *et al.* (1973), c_w is an O(1) constant. Internal wave effects can extend up to a maximum frequency of N where $N^2 = -g/\rho (\rho/z)$ and ρ is the fluid density (in wavenumber space this will correspond to a maximum wavenumber of $2\pi N/u$ where u is the sensor velocity relative to the water).

Inertial Convective Subrange

For scales smaller than $2\pi N/u$, but large enough to be influenced by viscosity, we have the inertial convective subrange. The temperature gradient spectrum in the inertial convective subrange is given by (Monin and Yaglom 1975, Vol 2, pg 479-485)

$$S_{ICS}(k) = c_{ICS} \chi_T \varepsilon^{-1/3} k^{1/3} \quad (6)$$

where c_{ICS} is an O(1) constant and χ_T is the dissipation of temperature variance due to turbulence and is defined for the case of isotropic turbulence by

$$\chi_T = 6 D_T \int_0^\infty S(k) dk = 6 D_T \overline{\left(\frac{T'}{z} \right)^2}, \quad (7)$$

where the overbar denotes an ensemble average, D_T is the diffusivity of heat and T' is the temperature fluctuation. The spectrum given by (6) is valid to a wavenumber $(c_{ICS}/c_{VC})^{3/2} k_k$

where the Kolmogorov wavenumber is $k_k = (\epsilon/\nu)^{1/4}$ and c_{VC} is a constant related to the spectrum in the viscous convective subrange (see below).

Batchelor spectrum

In his paper, Batchelor (1959) developed the form of the temperature gradient wavenumber spectrum for high Reynolds number, isotropic, homogeneous turbulence. Gibson and Schwartz (1963) used Batchelor's results to derive the one-dimensional Batchelor spectrum $S(k)$ of the temperature gradient

$$S(k) = \frac{\chi_T}{2 D_T} \frac{\sqrt{2q}}{k_B} S_N(\alpha), \quad (8)$$

where k has units of rad m^{-1} , q is a universal constant, Batchelor wavenumber k_B is defined as the inverse of the Batchelor length scale $L_B = (D_T^2 \nu/\epsilon)^{1/4}$, and α is a dimensionless wavenumber given by $(2q)^{1/2} k k_B^{-1}$. The normalised spectrum $S_N(\alpha)$ is given by

$$S_N(\alpha) = \alpha \left[e^{-\alpha^2/2} - \alpha \int_{\alpha}^{\infty} e^{-x^2/2} dx \right]. \quad (9)$$

The one-dimensional form $S(k)$ has been confirmed in laboratory experiments involving turbulence generated behind a grid (Gibson and Schwartz 1963), in the upper ocean (Dillon and Caldwell 1980) and in lakes (Imberger 1985).

The initial part of the Batchelor spectrum for $Pr = \nu/D_T > 1$ is the viscous convective subrange and is given by (Batchelor 1959, Gibson and Schwartz 1963)

$$S_{VC}(k) = c_{VC} \frac{\chi_T}{D_T} \frac{k}{k_B^2} \quad (10)$$

where c_{VC} is an $O(1)$ constant (Dillon and Caldwell, 1980; Oakey, 1982). Sherman and Davis (1995) have shown that the viscous-convective subrange is only found for events with large values of the Cox number $C_T = \chi_T/2D_T T_z^2$ where T_z is the mean temperature gradient. We shall refer to the portion of the Batchelor spectrum at wavenumbers higher than that of the spectral maximum as the roll-off region (see Fig. 1a).

The value of the universal constant q was estimated to be $3^{1/2} < q < 2(3^{1/2})$ from theoretical arguments advanced by Gibson (1968a, b). Grant *et al.* (1968) estimated $q = 3.9 \pm 1.5$ and Dillon and Caldwell (1980) used $q = 2(3^{1/2}) = 3.46$. Oakey (1982) determined $q = 3.67 \pm 1.52$ by comparing direct measurements of dissipation with those obtained from temperature gradient spectra. In this paper it is assumed that $q = 2(3^{1/2})$.

It should be noted that the Batchelor spectrum can be applied to any resolvable tracer that has a Prandtl reasonably greater than unity.

Noise Spectra

Noise is generated either at the sensor or by the processing circuitry. Typically, the noise spectrum will have a slope of around 2. The wavenumber at the intersection of the Batchelor and noise spectra is denoted k_n .

There have been various attempts to reduce the effects of noise. For example, Dillon and Caldwell (1980) used the in-phase power between redundantly amplified channels to reduce electronic noise. However, this technique is not necessarily useful for newer microstructure probes where electronic noise levels have been reduced resulting in sensor noise dominating electronic noise.

3. Data Requirements

Before Batchelor curve fitting can be used to determine dissipation it is usually necessary that: 1) the frozen field assumption be valid, 2) the temperature signal is corrected for the thermistor response, 3) stationary data segments are selected. The frozen field assumption or Taylor hypothesis (Taylor 1938) is used to convert the response of a thermistor from frequency ω to wavenumber k space using $k = \omega/u$, where the frequency ω is measured in radians per second and wavenumbers given in radians per metre. The Taylor hypothesis is generally considered to be valid if variations in the fluctuating velocities are small compared with u , the probe velocity relative to the fluid (see Townsend 1976, pg 67). Ideally, the probe speed will be reasonably greater than the largest turbulent velocity fluctuations but not so great that sensor roll-off becomes a problem. Given that $u \sim (\epsilon l)^{1/3}$ where u and l are the rms velocity and overturn size of the turbulence (Luketina and Imberger, 1989), and l is typically less than 0.1 m and ϵ around $10^{-5} \text{ m}^2 \text{ s}^{-3}$ in an energetic environment, results in $u \sim 10^{-2} \text{ m s}^{-1}$. Thus a probe velocity of 0.1 m s^{-1} is a good compromise between satisfying the frozen field requirement and minimising sensor roll-off. Higher probe velocities can be used in less energetic environments.

Because much of the spectral energy encountered by a thermistor is near the highest frequencies the thermistor can resolve, it is usually necessary to correct for the thermistor response. Generally, the response of a thermistor to changes in temperature is limited by the time for heat to diffuse through the boundary layer surrounding the sensor (Gregg and Meagher, 1980). Response functions and correction methods for fast response thermistors have been published by Gregg and Meagher (1980), Dillon and Caldwell (1980), Fozdar *et al.* (1985) and Sherman and Davis (1995). Here the method of Fozdar *et al.* (1985) is used.

It is necessary to divide the data into statistically stationary segments or intervals if the measured spectrum $D(k)$, or a portion of it, is to behave as a Batchelor spectrum (Imberger and Boashash, 1986). An example of this is provided in section 4; arbitrarily dividing the

data into short segments is not a guarantee that the turbulence is homogeneous within a segment.

Note that comments relating to measured spectra in subsequent sections of this paper refer to (wavenumber) band averaged spectra. The number of spectral points n_i averaged to form the i^{th} point in the band averaged spectrum is a geometric series with n_i increasing from low to high wavenumbers. Thus confidence in the accuracy of the spectral estimate increases with increasing wavenumber (see Bendat and Piersol, 1986, pg 285).

4. Method

When a theoretical Batchelor spectrum as given by (8) is fitted to a spectrum of known variance, the only free variable is the Batchelor wavenumber, which in turn, defines the dissipation. As mentioned previously, key issues in fitting the theoretical Batchelor curve are: 1) what is the appropriate portion of the measured spectrum to use, 2) how should the variance χ_T be determined from the measured spectrum, and 3) what is an appropriate error function to use in determining the optimum fit? These issues and other aspects of the method are discussed in this section.

Before proceeding, it should be noted that (8) applies to a spectrum based on radian wavenumbers k having units of rad m^{-1} . If the spectra being fitted are based on cyclical wavenumbers κ having units of m^{-1} then the non-dimensional wavenumber $\alpha = (2q)^{1/2} \kappa \kappa_B^{-1}$, where $\kappa_B = (2\pi L_B)^{-1}$. For the remainder of this paper we shall only deal with cyclical wavenumbers. The measured spectrum will be denoted $D(\kappa)$ to distinguish it from the theoretical or fitted spectrum $S(\kappa)$. The universal constant q in (7) is assumed to be $2(3)^{1/2}$ and the non-dimensional spectrum $S_N(\alpha)$ as defined in (9) is approximated by

$$S_N(\alpha) \approx \alpha [e^{-\alpha^2/2} - \sqrt{2\pi} \alpha Q(\alpha)], \quad (11)$$

where

$$\begin{aligned} Q(\alpha) &= \frac{1}{\sqrt{2\pi}} \int_{\alpha}^{\infty} e^{-x^2/2} dx \\ &\approx \frac{1}{\sqrt{2\pi}} e^{-\alpha^2/2} [.319381530 \alpha - .356563782 \alpha^2 + 1.781477937 \alpha^3 \\ &\quad - 1.821255978 \alpha^4 + 1.330274429 \alpha^5] \end{aligned} \quad (12)$$

and

$$\tau = (1 + .2316419 \alpha)^{-1} \quad (13)$$

(see Abramowitz and Stegun 1970 section 26.2.17). The dissipation of turbulent kinetic energy is then found by rearranging the definition of the Batchelor wavenumber to give

$$\varepsilon = (2\pi)^4 \nu D_T^2 \kappa_B^4. \quad (14)$$

Overview of Method

Once the variance χ_T is estimated, the theoretical spectrum $S(\kappa)$ can be fitted to the appropriate portion of the measured spectrum $D(\kappa)$ with the Batchelor wavenumber κ_B being the free variable. A non-linear curve fitting algorithm could be used to try to find the best fit (*ie* that with the least error). However, these algorithms often only find the best local rather than global fit. Further, they are computationally demanding. For this reason, the best fit was found using a trial and error approach. A trial consisted of finding the error in log-log space (the error function is discussed later) associated with a particular value of the Batchelor wavenumber κ_B . The wavenumber κ_B resulting in the least error for a set of trials is assumed to be the optimum fit for that set of trials. Up to six sets of trials take place with the noise wavenumber κ_n and the variance χ_T being progressively modified following each set of trials (see the following sub-section). The dissipation is found by substituting the wavenumber κ_B , associated with the best overall fit during the final three sets of trials, into (14).

A set of trials consists of using 200 geometrically spaced values of the wavenumber κ_B such that ε ranges from 10^{-12} to $10^{-4} \text{ m}^2 \text{ s}^{-3}$. However, if κ_B exceeds κ_n (the noise wavenumber) then the upper limit for κ_B is taken to be κ_n .

The fitting procedure is done in log-log space as spectra are commonly presented in this manner and the roll-off region is well defined compared with a linear-linear format.

There is no reason why the procedures that are presented here cannot be adapted for use with variance preserving spectra in a linear-linear format.

Determining Variance

For any portion of the measured spectrum between the limiting wavenumbers, κ_L and κ_n , the temperature variance dissipation χ_T is found from

$$\chi_T = 6 D_T \left[\int_0^{\kappa_L} S(\kappa) d\kappa + \int_{\kappa_L}^{\kappa_n} D(\kappa) d\kappa + \int_{\nu_n}^{\infty} S(\nu) d\nu \right] \quad (15)$$

where the molecular diffusivity of heat D_T for seawater can be estimated from formulae given in Fofonoff and Millard (1983).

Prior to the first set of trials, κ_L is set to the lowest wavenumber of the measured spectra $D(\kappa)$. For each subsequent set of trials, κ_L is the lowest wavenumber at which the measured spectra $D(\kappa)$ and the best fit theoretical spectra $S(\kappa)$ (from the previous set of fits) intersect (see Fig. 3) (if there is no intersection, κ_L does not change).

The noise wavenumber κ_n is initially set to the wavenumber corresponding to the spectral minimum at wavenumbers greater than 30 m^{-1} . This generally ensures that the appropriate minima is selected. However, in some instances, this estimate of κ_n may be too high. By comparing the best fit spectrum from the first set of trials with the measured spectrum it is possible to re-evaluate whether κ_n should be reduced. First, the highest wavenumber intersection of the theoretical (*i.e.* fitted) and measured spectra is found. The measured spectrum is then scanned in the direction of higher wavenumbers until a positive gradient, indicating noise, is encountered. If this wavenumber is less than the previous value of the noise wavenumber κ_n , κ_n is replaced. This is only done at the end of the first set of trials and prior to the second set of trials.

Which portion of the measured spectrum should be used

Once wavenumbers higher than κ_n have been excluded, the only basis for determining the Batchelor portion of the measured spectrum is that it is shaped like a Batchelor spectrum. Accordingly, different portions of the data between the lowest wavenumber of the measured spectrum and the noise wavenumber κ_n are fitted. These portions extend from κ_1 to κ_2 where all possible κ_1 and κ_2 are tried subject to:

$$\begin{aligned}\kappa_1 &< \kappa_{\text{peak}} , \\ \kappa_2 &> 3 \kappa_{\text{peak}} , \\ \log_{10} \kappa_2 - \log_{10} \kappa_1 &> 0.8 ,\end{aligned}\tag{16}$$

where the peak of the theoretical spectrum is $S(\kappa_{\text{peak}})$ where κ_{peak} is equal to $0.176 \kappa_B$. Potential values of κ_1 and κ_2 satisfying the first two criteria are shown in Fig. 3.

The restrictions given in (16) ensure that at least the peak of the spectrum and the initial part of the roll-off region are included in the fitting. Further, the wavenumbers of the data being fitted must span not much less than a decade.

error function

The standard approach would be to specify the fitting error based on the difference between the theoretical and measured spectrum at each wavenumber. This approach was only found to be successful using a relatively complicated error function (Luketina, 1987). The key to a more robust error function is to recognise that once χ_T is specified, the theoretical curve as given by (8) is constrained to move along a slope of -1 in log-log space. For this reason, when working in log-log space, as is done here, the error should be the difference between the theoretical and measured spectrum in the direction of slope -1 (see Fig. 4).

The error function is a modified least squares type in log space, given by

$$\delta_e = \frac{1}{f_r^c} \sum_{i=1}^m \lambda_i \frac{w_i}{(m-1)} \quad (17)$$

where w_i is a weight based on the number of raw spectral data points band averaged to produce $D(\kappa_i)$, m is the number of data points (after band averaging) between wavenumbers κ_1 and κ_2 , $m-1$ is the number of degrees of freedom, f_r is the fraction of the maximum possible number of data points used (*i.e.* all those at wavenumbers lower than κ_n), c is a constant, and

$$\lambda_i^2 = (\log D(\kappa_i) - \log S(\kappa_{Si}))^2 + (\log \kappa_i - \log \kappa_{Si})^2, \quad (18)$$

where $S(\kappa_{Si})$ is the point on the theoretical spectrum that lies on the -1 slope passing through $D(\kappa_i)$ (see Figure 4).

The use of f_r^c biases the fitting procedure towards accepting a larger portion of the spectrum. Setting c to 1.5 has been found to give the best fits to a wide range of measured spectra (the procedure is not sensitive to the value of c if the measured spectrum is clearly Batchelor shaped). Dividing by $(m-1)$ is a standard normalisation. The weights w_i are based on the standard deviation of n_i points band averaged to a single point being reduced by a factor of $(n_i)^{-1/2}$. More specifically, the weights are calculated using $w_i = (n_i)^{-1/2}$ and are then multiplied by a factor so that the average value of the weights is unity.

It now remains to find $S(\kappa_{Si})$, or more specifically κ_{Si} . The method is illustrated in Figure 4 and is presented in terms of the normalised wavenumber $\alpha_{Si} = (2q)^{1/2} \kappa_{Si}/\kappa_B$. Figure 4 shows a data point α_i , $D_N(\alpha_i)$ on the normalised spectrum through which passes a line $L_N(\alpha)$ of slope -1 . The normalised spectrum is given by

$$D_N(\alpha) = \frac{2 D_T}{\chi_T} \frac{\kappa_B}{\sqrt{2q}} D(k). \quad (19)$$

Also shown is the normalised theoretical spectrum $S_N(\alpha)$ with the -1 tangent point $\alpha_{\text{tan}}, S_N(\alpha_{\text{tan}})$ indicated. Note that $\alpha_{\text{tan}} = 1.036$. A parameter Δ is defined as:

$$\Delta = \log S_N(\alpha) - \log L_N(\alpha) \quad (20)$$

We can now approximate the points α_{left} and α_{right} for $\Delta > 0$ using

$$\begin{aligned} \alpha_{\text{left}} &= -\log^{-1} \left[0.00469997 \zeta^3 + 0.0245363 \zeta^2 + 0.30571 \zeta - 0.101354 \right] \\ \alpha_{\text{right}} &= \log^{-1} \left[-0.00121412 \zeta^3 - 0.00956552 \zeta^2 + 0.152992 \zeta - 0.370123 \right] \end{aligned} \quad (21)$$

where $\zeta = \ln \Delta$. The wavenumber α_{Si} is then taken to be the closer of α_{left} and α_{right} (in the example of Fig. 4, $\alpha_{\text{Si}} = \alpha_{\text{left}}$) or, if $\Delta < 0$ (*ie* the line and fitted curve do not intersect), α_{Si} is set equal to α_{tan} .

5. Discussion

Examples of fitting to data

Figures 5 and 6 show the results of applying the curve fitting algorithm to a range of temperature gradient microstructure data. Figure 5 shows relatively good fits while Figure 6 shows relatively poor fits. These poorer fits are due to the measured spectrum lacking a clear Batchelor shaped region. The value of the fitting error δ_e as a function of dissipation is also shown. It can be seen that the error function has a unique minimum for a measured spectrum that is clearly Batchelor shaped. As the measured spectrum becomes less Batchelor like, the minimum in the error tends to be flatter, indicating that the uncertainty in the value of the dissipation is increased. In general, poor Batchelor fits result in higher values of the minimum error and the error curve shape deviating from the shapes shown in Figure 5 – either by being flatter in the region of the minimum or more irregularly shaped.

Overall, the algorithm has proven itself to be robust in selecting the Batchelor portion of the temperature gradient spectrum. In measured spectra where there is a clear Batchelor portion, the placement of the theoretical Batchelor spectrum is always close to the best fit 'by eye'.

Accuracy

The most accurate curve fitting, and hence dissipation estimates, will be when the measured spectrum is free of noise, finestructure and internal waves. Nonetheless, there will still be inaccuracies due to the fitting procedure, because each spectrum is only a sample of a larger population, and because the Nyquist wavenumber limits the highest wavenumber that can be resolved. These inaccuracies were assessed by using the Batchelor fitting technique on spectra derived from an artificial time series. The discrete artificial time series $\eta(t_i)$ was calculated using

$$\eta(t) = \sum_{j=1}^p A_j \sin(2\pi \kappa_j u \Delta t + \theta_j) \quad (22)$$

where θ_j is a uniformly distributed random variable in the range 0 to 2π , p is the number of wavenumber (or Fourier) components being used to simulate $\eta(t)$ and $\kappa_j = (j/p) \Delta\kappa$, where $\Delta\kappa = (2p \Delta t u)$ where Δt is the sampling interval of the time series. The magnitude of the component associated with wavenumber κ_j is

$$A_j = \left(2S(\kappa_j)\Delta\kappa\right)^{1/2}, \quad (23)$$

where $S(\kappa)$ is given by (8). The above relationships ensure that spectra taken from the time series will not be aliased as there is no energy in the time series above the Nyquist frequency.

Values of D_T , p , Δt and u were fixed as $1.4 \times 10^{-7} \text{ m}^2 \text{ s}^{-1}$, 300, 0.01 s and 0.1 m s⁻¹ respectively. This left ε and χ_T to be specified so that a time series could be generated. Spectra were then derived by using adjacent segments of duration τ (or record length $L_r = u\tau$) from a time series consisting of 51200 points. Statistical quantities calculated for the log of the Batchelor fitted estimates of dissipation were the mean $\mu_{\log \varepsilon}$ and the standard deviation $s_{\log \varepsilon}$. The originally specified dissipation was denoted ε .

Examples of artificially generated spectra and curve fits are shown in Figure 7 for a range of dissipations. The segment length (in this instance 0.512 m) limits the amount of the low wavenumber data which can be captured while the sampling interval ($\Delta t = 0.01$ s which corresponds to 1 mm in space) limits the highest wavenumber to 500 m⁻¹. The viscous-convective subrange is absent from the low dissipation spectrum due to the low wavenumber restriction while the roll-off region is only just discernable for the high dissipation spectrum due to the high wavenumber limit.

Figure 8 shows the relationship between the actual ϵ and mean of the dissipation estimates $\mu_{\log \epsilon}$ in the form of a percentage error $100 (\log \epsilon - \mu_{\log \epsilon}) / \log \epsilon$. It is clear that the estimated and actual values are in good agreement in the range 10^{-9} to $10^{-5} \text{ m}^2 \text{ s}^{-3}$. Below $10^{-9} \text{ m}^2 \text{ s}^{-3}$, dissipation tends to be underestimated due to the limitation of data in the viscous-convective subrange while above $10^{-5} \text{ m}^2 \text{ s}^{-3}$, dissipation tends to be overestimated, due to little data in the roll-off region. Figure 8 shows that the systematic error in the mean of the low (*ie* less than 10^{-9}) dissipation estimates is more than 5% when $\kappa_B / \kappa_n < 3.2$ where $\kappa_r = L_r^{-1}$. At high values of dissipation (*ie* more than 10^{-5}) the systematic error is generally larger than 5%. There is a slight reduction in the error as the record length is increased. Systematic errors can be corrected using Fig. 8.

In the field, there is rarely an opportunity to average large numbers of dissipation estimates. In this case, we are concerned with the likely error or standard deviation of a single dissipation estimate. Figure 9 shows the highest random error occurs at high values of dissipation due to the roll-off region not being resolved. However, the error reduces as the record length increases. More specifically, the random error associated with the log dissipation estimates is more than 5% for $\kappa_B / \kappa_n^{-2/3} > 600$.

Statistical Stationarity

Dillon and Caldwell (1980) claimed that dissipation estimates in non-stationary regions would be biased towards the higher dissipation values in the sample. In other words, the estimated dissipation would be greater than the volume averaged dissipation of the sample. Here we examine this assertion using artificially generated non-stationary data sets. More specifically, 2048 sample time (or depth) series was generated such that each half of the data set had different values of dissipation. Fig. 10 shows spectra of two of these artificial time series. From examining Fig. 10 it is evident that the spectrum for the entire profile (*ie* 2048 sample data set) basically follows the spectrum of the lower dissipation portion of the profile at low wavenumbers and vice-versa at high wavenumbers. In general, the spectrum of

a temperature gradient profile with several statistically stationary regions is equivalent to taking, at each wavenumber, the average of the spectra for each stationary region. This is one reason why measured temperature gradient spectra may not be close in shape to the theoretical Batchelor spectrum.

The ratio of the estimated dissipation ϵ_B and the volume averaged dissipation ϵ_{vol} was calculated for a number of the artificial non-stationary data sets. The results are plotted in Fig. 11 where it can be seen that dissipation is overestimated at low values of ϵ_{vol} and underestimated at high values of ϵ_{vol} . This occurs because the low ϵ_{vol} spectra are well resolved (ie the roll-off region is well defined) as in Fig. 10b while the high ϵ_{vol} spectra are dominated by the viscous-convective region (eg Fig. 10a). These results are consistent with Dillon and Caldwell's (1980) assertion that dissipation estimates in non-stationary regions would be biased towards the higher dissipation values in the sample because they were only using well-resolved spectra.

The dissipation value at which we switch from underestimating to overestimating dissipation will depend upon the bandwidth of the measured spectra. In turn, the bandwidth will depend upon the sampling frequency and the record length L_r . The presence of finestructure and internal waves will affect the effective bandwidth due to the fitting algorithm rejecting the lower wavenumber portion of the spectrum; this will tend to result in dissipation being overestimated rather than underestimated.

The biasing of dissipation estimates in non-stationary regions highlights the importance of being able to divide or segment data into stationary regions prior to estimating dissipation. To demonstrate that such segmentation is viable we have applied the segmentation algorithm of Imberger and Ivey (1991) to one of the artificially generated non-stationary temperature gradient data sets (see Fig. 12). The segmentation parameter shown in Fig. 12b has a large value wherever there is an appreciable change in the frequency content of the signal (the artificially generated data set changes from $\epsilon = 10^{-6}$ to $\epsilon = 10^{-7} \text{ m}^2 \text{ s}^{-3}$ at its

mid-point). In particular, that the largest value of the segmentation parameter occurs at the mid-point transition. Thus, selecting a threshold of, say, 100 for the segmentation parameter would result in a segmentation boundary being placed at the transition; thereby dividing the data into stationary regions.

6. Conclusions

A relatively robust method for determining dissipation from Batchelor curve fitting has been described. Overall, the use of the method to determine dissipation results in considerable time savings when compared to manual methods. The systematic and random errors associated with determining the dissipation have been shown to be a function of the dissipation and the record length. Of course, these errors are the best case, as the presence of internal waves and finestructure will result in increased errors.

ACKNOWLEDGEMENTS

We would like to thank Greg Ivey and Mike Barry for providing constructive comments on an initial draft of this paper. Angelo Saggio provided the data shown and Carol Lam checked the coding of the algorithm. This work forms WRL reference 198 and CWR reference ED648DL.

REFERENCES

Abramowitz, M., and I. A. Stegun, 1970: *Handbook of Mathematical Functions*, Dover Publications Inc., New York, 1046 pp.

Batchelor, G. K., 1959: Small-scale variations of convected quantities like temperature in turbulent fluid. Part 1: General discussion and the case of small conductivity. *J. Fluid Mech.*, **5**, 113-133.

Bendat, J. S., and A. G. Piersol, 1986. *Random Data - Analysis and Measurement Procedures*, 2nd Edition, Wiley-Interscience, New York, 566 pp.

De silva, I. P. D., Imberger, J. and G. I. Ivey, 1997. Localised mixing due to a breaking internal wave ray at a sloping bed, *J. Fluid Mech.*, **350**, 1-27.

Dillon, T. M., 1982: Vertical overturns: a comparison of Thorpe and Ozmidov length scales, *J. Geophys. Res.*, **87**(C12), 9601-9613.

Dillon, T. M., and D. R. Caldwell, 1980: The Batchelor spectrum and dissipation in the upper ocean. *J. Geophys. Res.*, **85**, 1910-1916.

Fofonoff, N. P., and R. C. Millard Jr., 1983: *Algorithms for Computation of Fundamental Properties of Seawater*, UNESCO Technical Paper in Marine Sciences No. 44.

Fozdar, F. M., Parker, G.J., and J. Imberger, 1985: Matching temperature and conductivity sensor response characteristics. *J. Phys. Oceanogr.*, **15**, 1557-1569.

Gibson, C. H., 1968a: Fine structure of scalar fields mixed by turbulence. Part I: Zero-gradient points and minimal-gradient surfaces. *Phys. Fluids*, **11**, 2305-2315.

Gibson, C. H., 1968b: Fine structure of scalar fields mixed by turbulence. Part II: Spectral theory. *Phys. Fluids*, **11**, 2305-2315.

Gibson, C. H., and W. H. Schwartz, 1963: The universal equilibrium spectra of turbulent velocity and scalar fields, *J. Fluid. Mech.*, **16**, 365-384.

Grant, H. L., Hughes, B. A., W. M. Vogel, and A. Moilliet, 1968: The spectrum of temperature fluctuations in turbulent flow. *J. Fluid Mech.*, **34**(3),423-442.

Gregg, M. C., 1977a: Variations in the intensity of small scale mixing in the main thermocline. *J. Phys. Oceanogr.*, **7**, 436-454.

Gregg, M. C., 1977b: A comparison of finestructure spectra from the main thermocline. *J. Phys. Oceanogr.*, **7**, 33-40.

Gregg, M. C., Cox, C. S., and P. W. Hacker, 1973: Vertical microstructure measurements in the central North Pacific, *J. Phys. Oceanogr.*, **3**, 458-469.

Gregg, M. C., D'Asaro, E. A., Shay, T. J., and N. Larson, 1986: Observations of persistent mixing and near-inertial waves, *J. Phys. Oceanogr.*, **16**(5), 856-884.

Gregg, M. C., and T. B. Meagher, 1980: The dynamic response of glass rod thermistors, *J. Geophys. Res.*, **85**(C5), 2779-2786.

Gregg, M. C., Winkel, D. P., and T. B. Sanford, 1991: Dissipation and the vertical wavenumber spectra of internal waves in the oceanic thermocline, *Proceedings of the Eighth Conference on Atmospheric and Oceanic Waves and Stability*, October 14-18, Denver, Colorado.

Imberger, J., 1985: The diurnal mixed layer, *Limnol. Oceanogr.*, **30**(4), 737-770.

Imberger, J., and B. Boashash, 1986: Application of the Wigner-Ville distribution to temperature gradient microstructure: a new technique to study small-scale variations, *J. Phys. Oceanogr.*, **16**(12), 1997-2012.

Imberger, J., and G. N. Ivey, 1991: On the nature of turbulence in a stratified fluid. Part 2: Application to lakes. *J. Phys. Oceanogr.*, **21**(5), 659-679.

Ivey, G. N., and J. Imberger, 1991: On the nature of turbulence in a stratified fluid. Part 1: The energetics of mixing. *J. Phys. Oceanogr.*, **21**(5), 650-658.

Kolmogorov, A. N., 1941: The local structure of turbulence in an incompressible viscous fluid for a very large Reynolds number. *C. R. Acad. Sci. USSR*, **30**, 301-305.

Luketina, D. A., 1987: *Frontogenesis of freshwater overflows*. PhD thesis, University of Western Australia.

Luketina, D. A., and J. Imberger, 1989: Turbulence and entrainment in a buoyant surface plume. *J. Geophys. Res.*, **94**(C9), 12619-12636.

Monin, A. S., and A. M. Yaglom, 1975. *Statistical Fluid Mechanics*, Vol. 2, 3rd edition, MIT press, 1987, 874 pp.

Oakey, N. S., 1982: Determination of the rate of dissipation of turbulent kinetic energy from simultaneous temperature and velocity shear microstructure measurements. *J. Phys. Oceanogr.*, **12**, 256-271.

Osborn, T. R., 1980: Estimates of the local rate of vertical diffusion from dissipation estimates. *J. Phys. Oceanogr.*, **10**, 83-89.

Pedlosky, J., 1987: *Geophysical Fluid Dynamics*, Springer Verlag, 710 pp.

Press, W. H., Flannery, B. P., Teukolsky, S. A., and W. T. Vetterling, 1989. *Numerical Recipes - The Art of Scientific Computing (FORTRAN Version)*, Cambridge University Press, 1990, 702 pp.

Saggio, A., and J. Imberger, 1999, Mixing and turbulent fluxes in the metalimnion of a stratified lake. submitted to *J. Geophys. Res.*

Stewart, R. W., and H. L. Grant, 1962: Determination of the rate of dissipation of turbulent kinetic energy near the sea surface in the presence of waves. *J. Geophys. Res.*, **62**, 3177-3180.

Sherman, J. T., and R. E. Davis, 1995: Observations of temperature microstructure in NATRE. *J. Phys. Oceanogr.*, **25**, 1913-1929.

Taylor, G. I., 1938: The spectrum of turbulence. *Proc. Roy. Soc. Lond.*, **A164**, 476-490.

Teoh, S. G., Ivey, G. I., and J. Imberger, 1997. Laboratory study of the interactions between two internal wave rays, *J. Fluid Mech.*, **336**, 91-122.

Townsend, A. A., 1976: *The Structure of Turbulent Shear Flow*. Cambridge University Press, 429 pp.

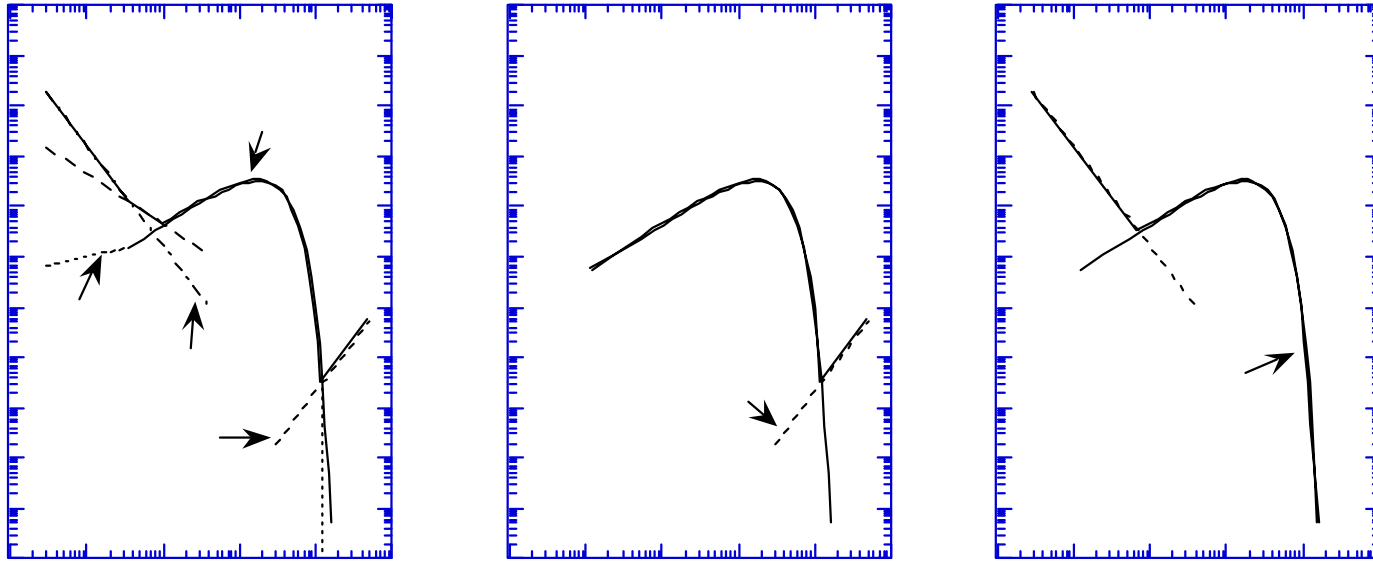


Fig. 1 A schematic showing the various processes contributing to the temperature gradient spectrum as a function of cyclic wavenumber κ . In a) contributing processes shown are: internal waves (dashed line at low wavenumbers), finestructure (dashed and dotted line), the inertial convective subrange (dotted line at low wavenumbers), the Batchelor spectrum (thin line) and thermal/electronic noise (dashed line at high wavenumbers). In b) an example is shown of a spectrum where internal wave, finestructure and ICS contributions are negligible. Such a spectrum may be found where there is energetic turbulence and weak stratification such as in a wind mixed layer. In c) a spectrum is sketched for the case where the finestructure contains a significant amount of energy at the lower wavenumbers. This type of spectrum may be found, for

example, in a stratified thermocline. Note that the thick lines in a), b) and c) represent the composite (*i.e.* measured) temperature gradient spectrum.

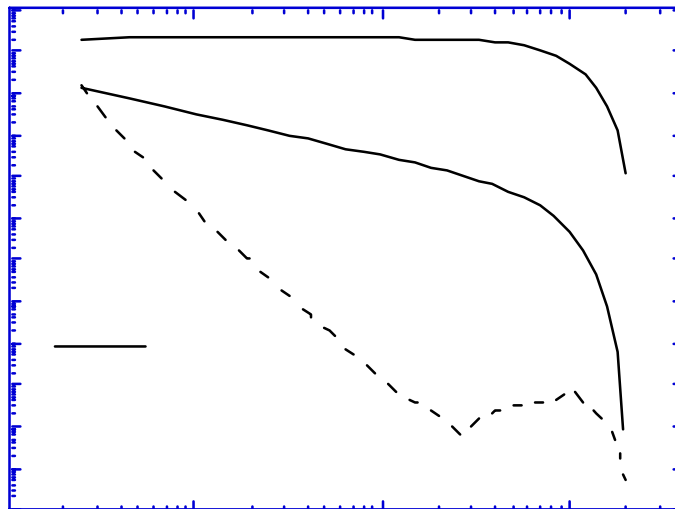
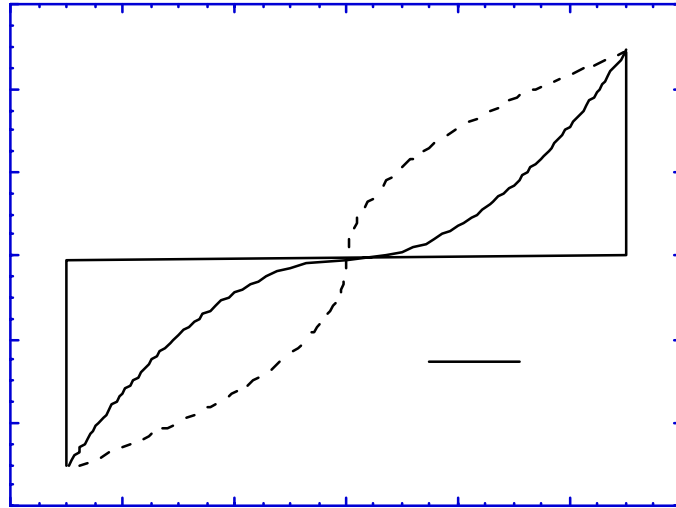


Fig. 2 Statically stable temperature profiles 1 m long with a 1 °C change from top to bottom in a) which satisfy Eq. (1) with $\gamma = 0$ (thin line), $\gamma = 0.5$ (thick line) and $\gamma = 2$ (dashed line) and b) the corresponding spectra of the temperature gradients.

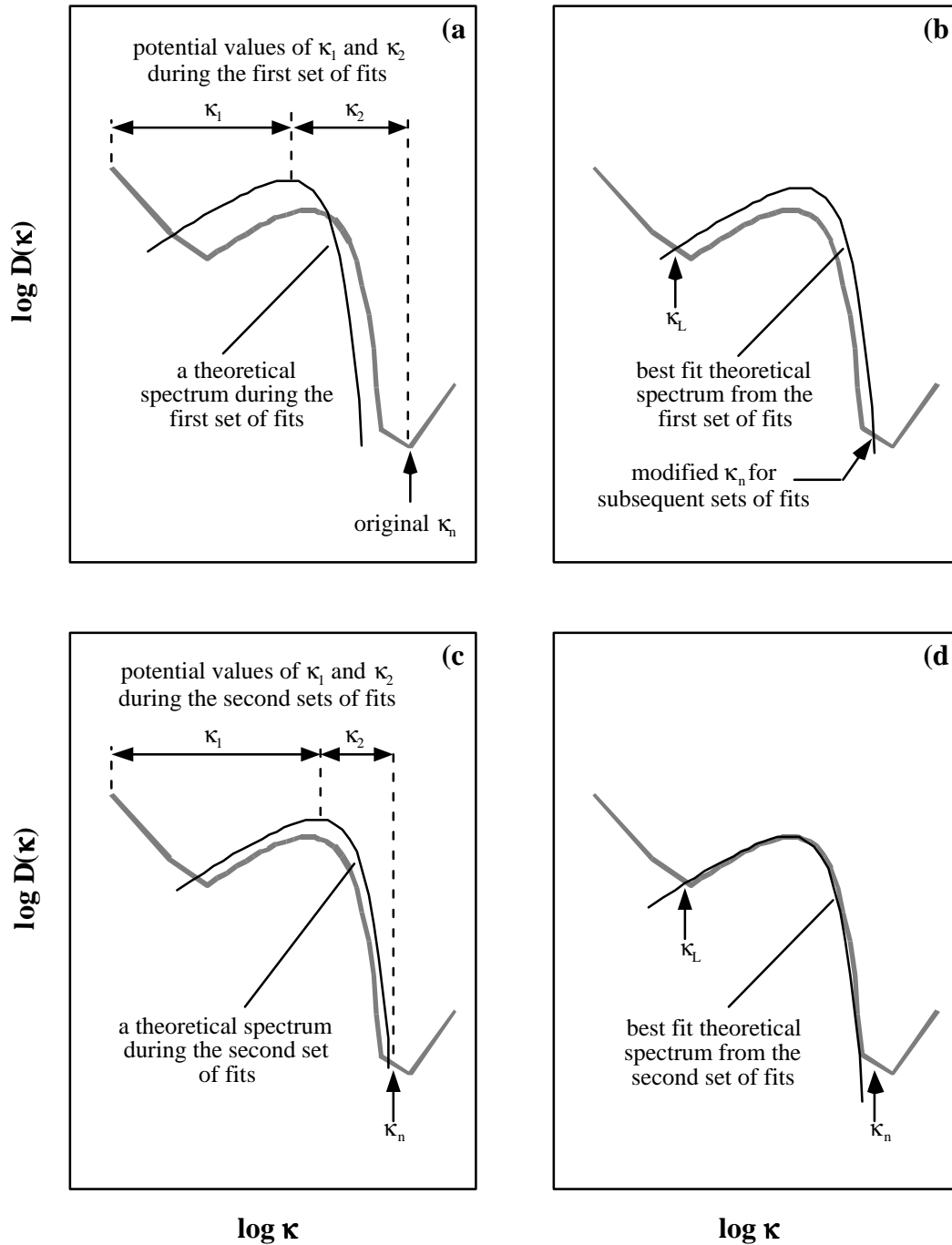


Fig. 3 A schematic showing the various stages in fitting a Batchelor spectrum (dark line) to a measured spectrum (grey line) to determine the kinetic energy dissipation ε . The dashed vertical line indicates the noise wavenumber κ_n . In a) the potential range of the wavenumbers κ_1 and κ_2 are indicated for a Batchelor spectrum being fitted during the first set of fits. Following the first set of fits, the wavenumber κ_L is determined and the noise wavenumber κ_n modified as shown in b). In c) the potential range of the wavenumbers κ_1 and κ_2 are indicated for a Batchelor spectrum being fitted during the second set of fits. Following the second set of fits, the wavenumber κ_L is modified as shown in d). Subsequent sets of fits repeat the procedure shown in c) and d), resulting in the wavenumber κ_L being progressively modified.

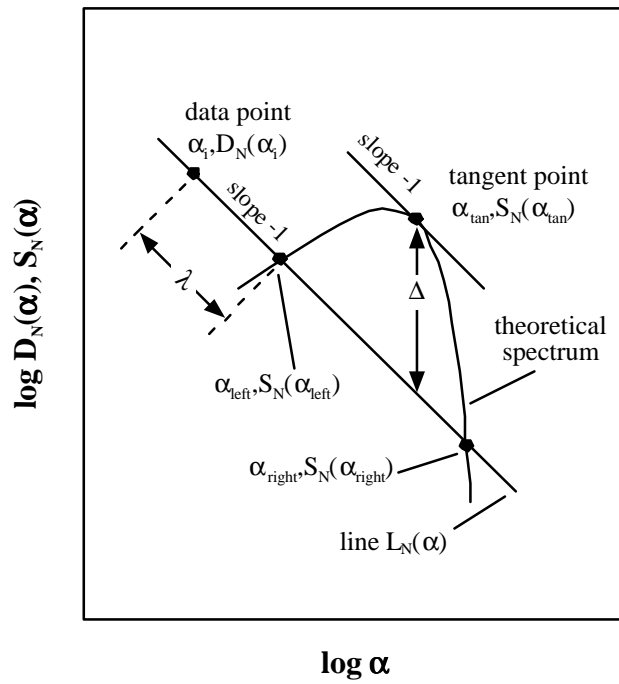


Fig. 4 Finding the deviation between a data point on the normalised measured spectrum and the normalised theoretical spectrum along a slope of -1 .

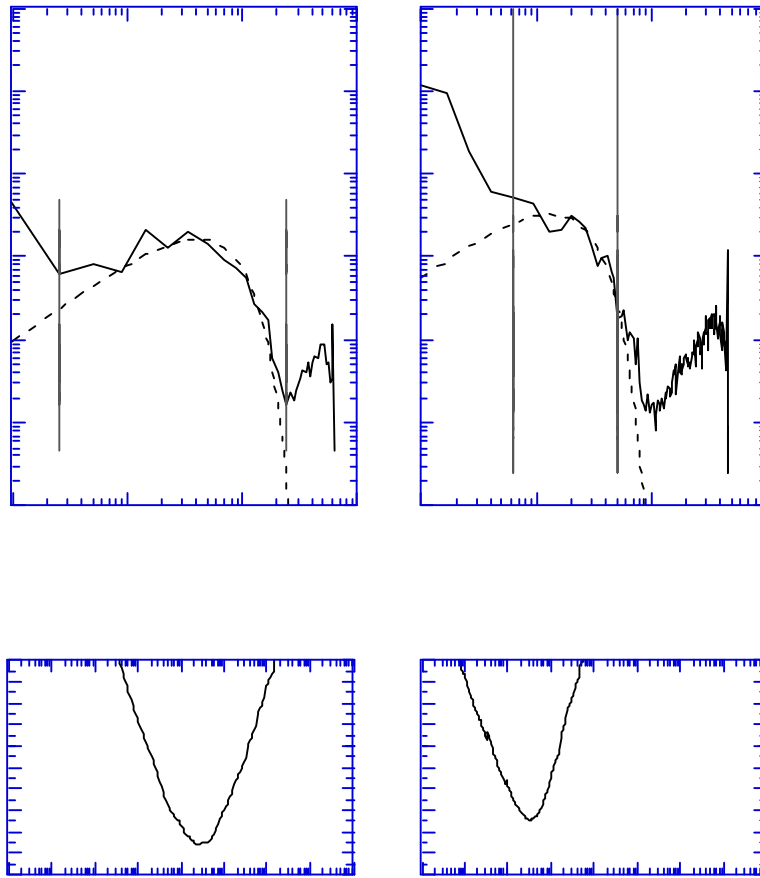


Fig. 5 Measured temperature gradient spectra $D(\kappa)$ (solid line) and fitted theoretical Batchelor spectra $S(\kappa)$ (dashed line) for data from a single profile in Lake Kinneret, Israel. The portion of the measured spectra that was used for fitting is between the two grey vertical lines. In a) the measured spectrum follows the theoretical form fairly well. In c) the curve fitting algorithm has ignored finescale/internal wave contamination at the low wavenumbers. In both cases the the algorithm has successfully fitted the Batchelor spectrum despite the presence of high frequency noise. Note that the noise decreases at the very high wavenumbers due to the use of a brickwall filter on the time series prior to the spectra being calculated. The fitting error δ_ϵ as a function of dissipation ϵ for cases a) and c) is shown in b) and d) respectively. In both cases there is an clear minima in the error function.

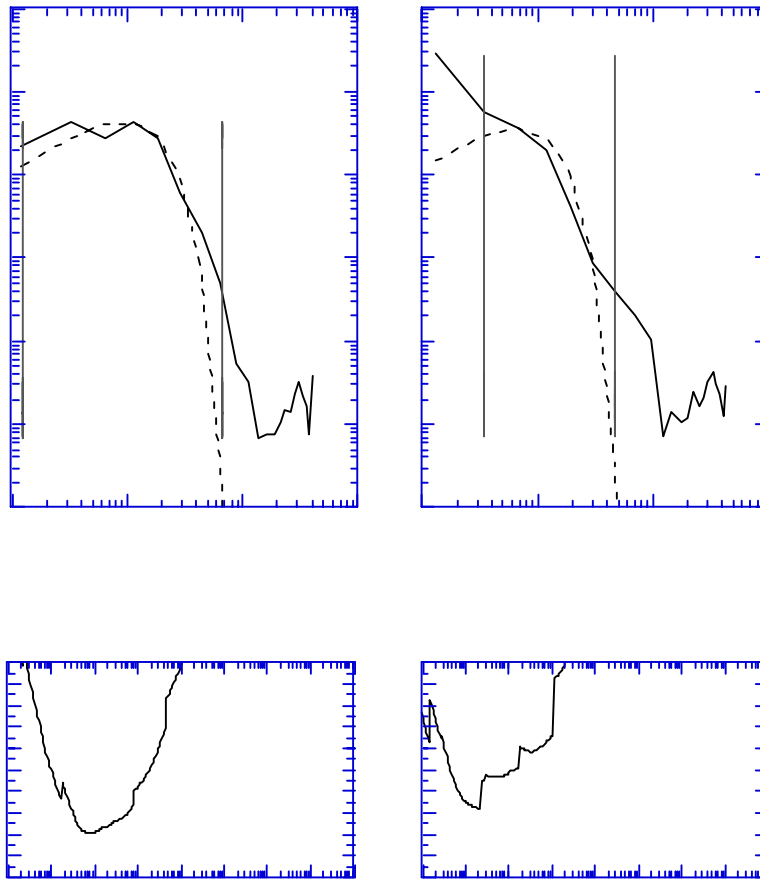


Fig. 6 See figure 5 for explanation of the different lines and symbols. In a) the measured spectrum does not follow the theoretical form very well. Consequently, the corresponding error function shown in b) is flatter in the region of the minima, and the value of the minima is larger than that for the more Batchelor shaped measured spectra of figure 5. In c) there is no discernable Batchelor shape. As a result, the the error function shown in d) is lacking the smoother shape shown in error graphs of figure 5. Further, the minimum error is relatively high.

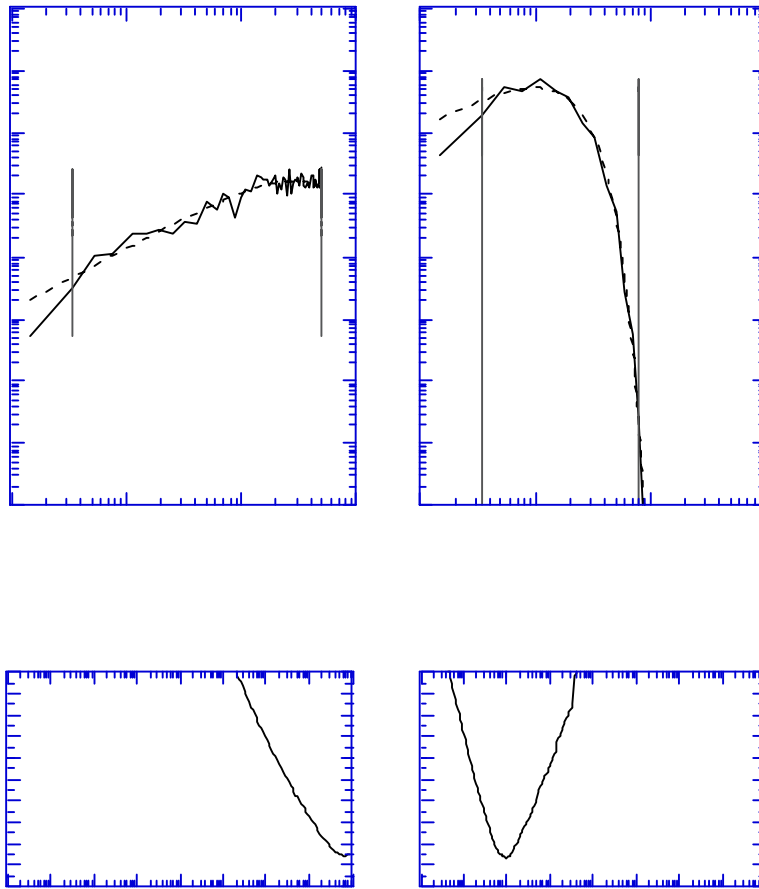


Fig. 7 Band averaged spectra corresponding to a) artificially generated data set 2048 samples long, the first half of the data set has $\varepsilon = 10^{-4} \text{ m}^2 \text{ s}^{-3}$ while the second half of the data set has $\varepsilon = 10^{-5} \text{ m}^2 \text{ s}^{-3}$, b) is similar except that $\varepsilon = 10^{-10} \text{ m}^2 \text{ s}^{-3}$ and $10^{-11} \text{ m}^2 \text{ s}^{-3}$ for the first and second parts of the data set. The different lines and symbols are explained in Fig. 5.

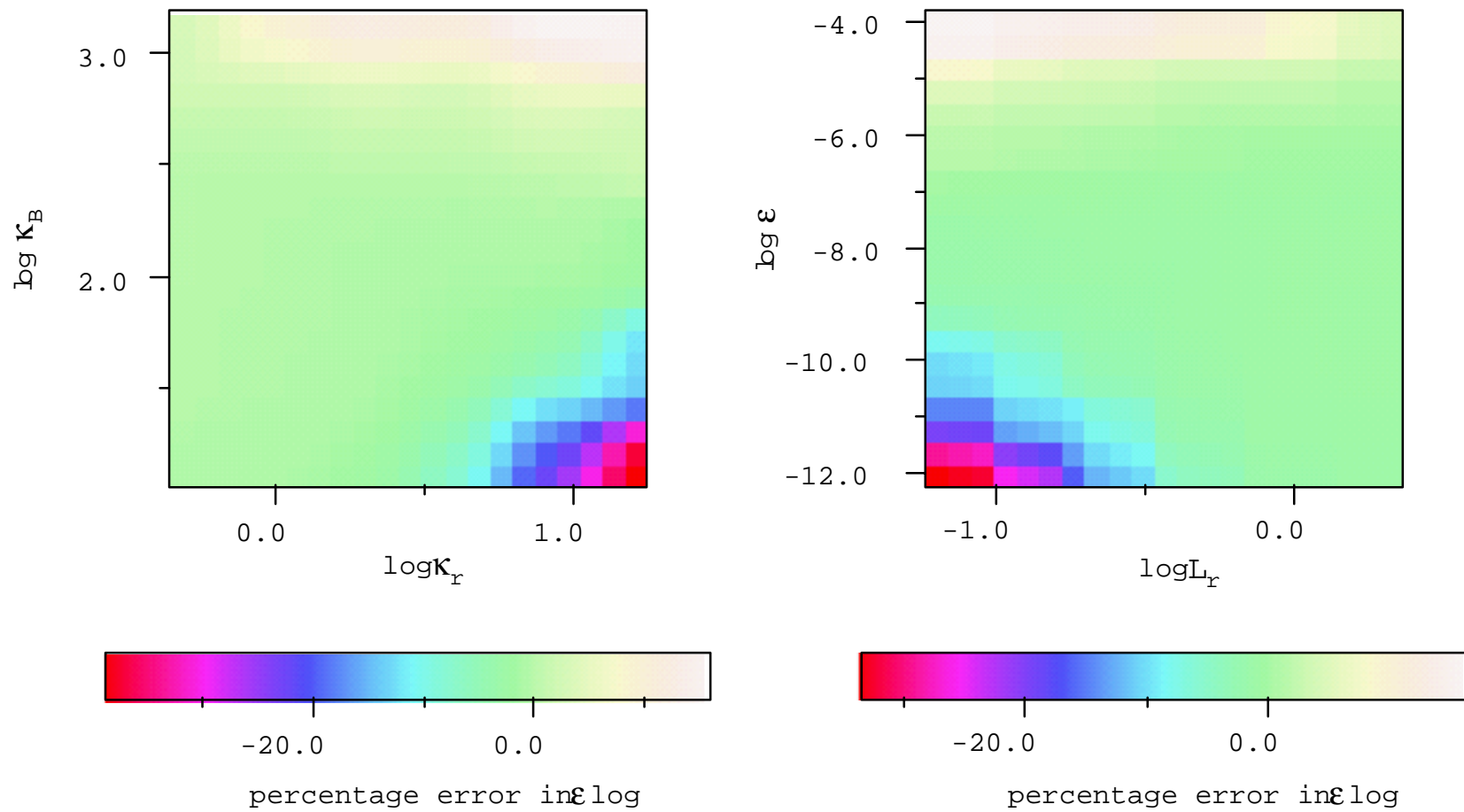


Fig. 8 Systematic error in estimates of log dissipation as a function of a) Batchelor wavenumber κ_B (based on actual dissipation) and record wavenumber κ_r which is the reciprocal of the record length and, b) actual dissipation and record length L_r .

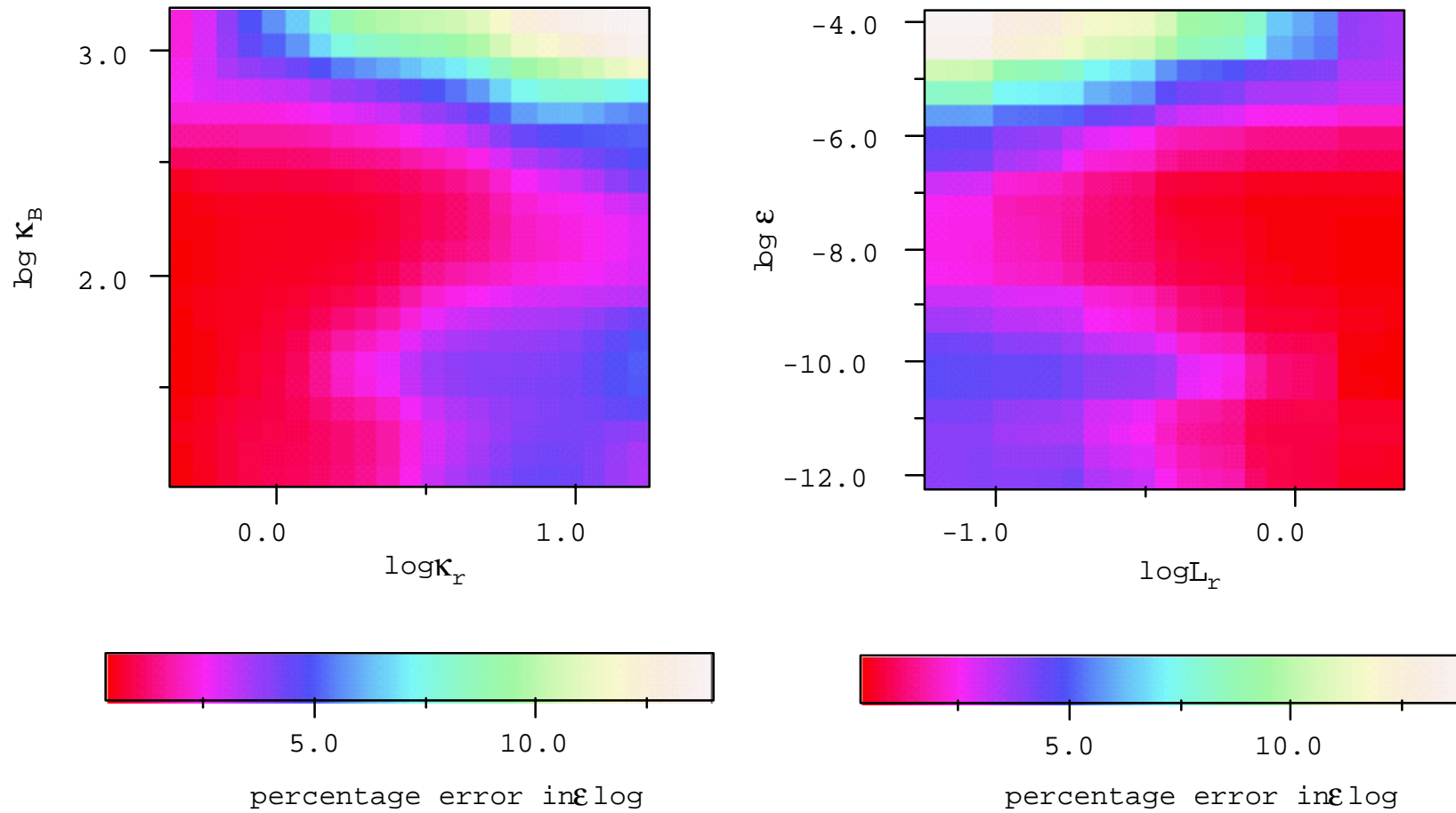


Fig. 9 Absolute value of the random error (standard deviation) in estimates of log dissipation as a function of a) Batchelor wavenumber κ_B (based on actual dissipation) and record wavenumber κ_r which is the reciprocal of the record length and, b) actual dissipation and record length L_r .

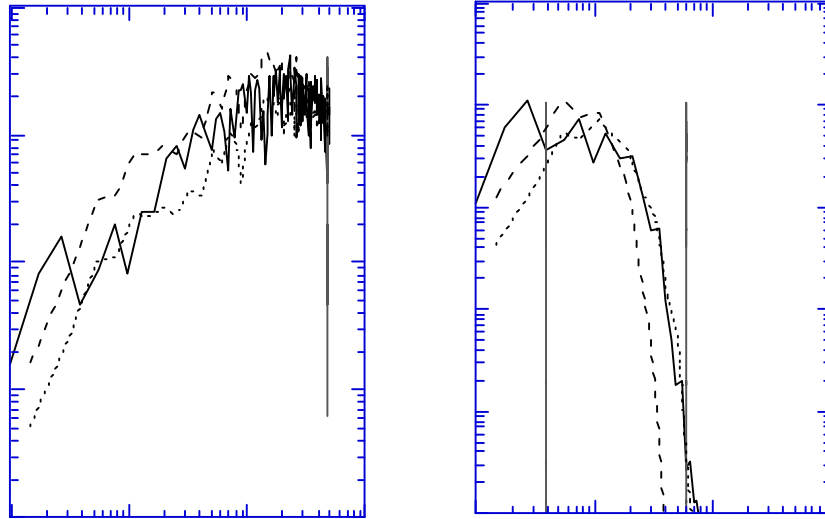


Fig. 10 Band averaged spectra corresponding to a) artificially generated data set 2048 samples long (solid line), the first half of the data set (line with short dashes) which has $\varepsilon = 10^{-4} \text{ m}^2 \text{ s}^{-3}$ and the second half of the data set (line with long dashes) which $\varepsilon = 10^{-5} \text{ m}^2 \text{ s}^{-3}$, b) is similar except that $\varepsilon = 10^{-10} \text{ m}^2 \text{ s}^{-3}$ (line with short dashes) and $\varepsilon = 10^{-11} \text{ m}^2 \text{ s}^{-3}$ (line with long dashes).

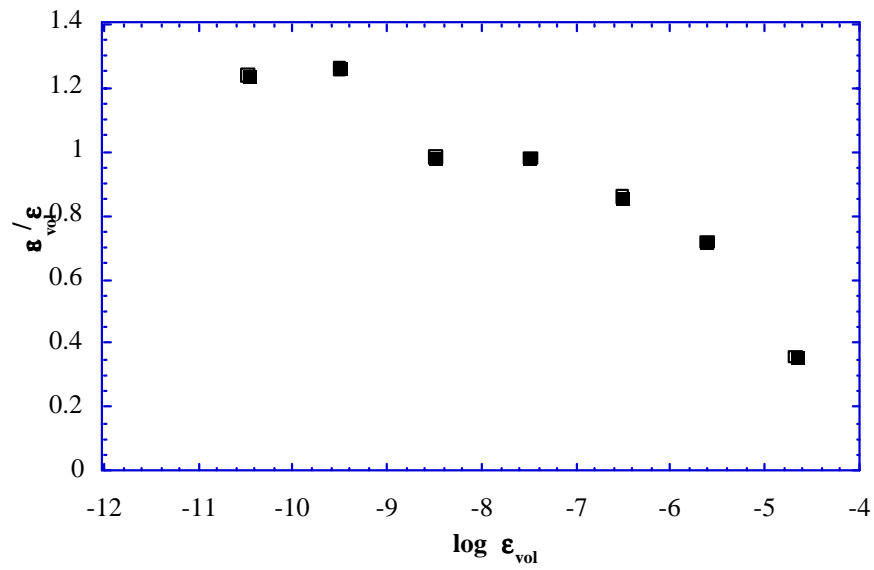


Fig. 11 Ratio of estimated dissipation ϵ_B to actual (volume averaged) ϵ_{vol} dissipation as a function of ϵ_{vol} when the data is non-stationary.

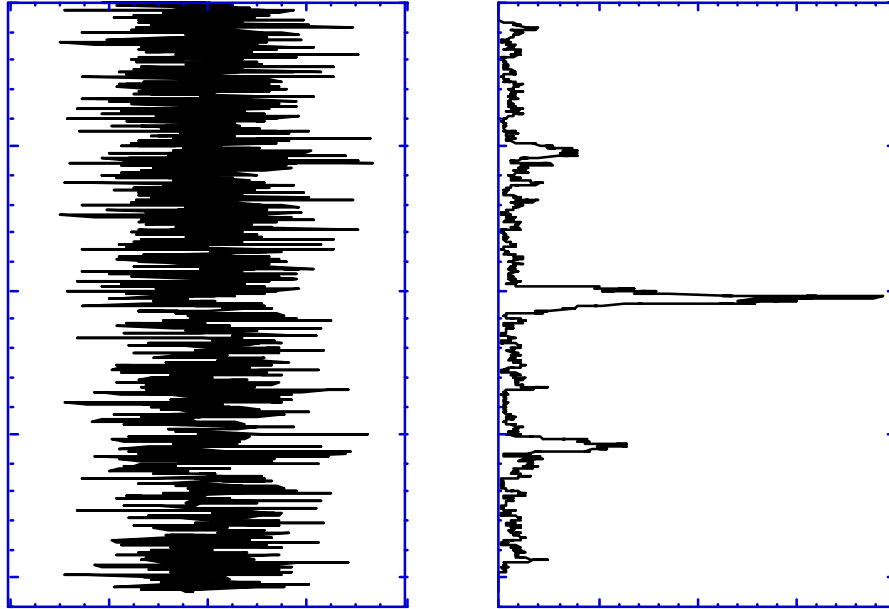


Fig. 12 Segmentation of a non-stationary data set: a) an artificially generated temperature gradient data set 2048 samples long where the upper and lower halves have $\varepsilon = 10^{-6} \text{ m}^2 \text{ s}^{-3}$ and $\varepsilon = 10^{-7} \text{ m}^2 \text{ s}^{-3}$ respectively and b) the corresponding segmentation parameter calculated using the method of Imberger and Ivey (1991). The dashed line in b) shows an arbitrary threshold of 100 which would result in a segmentation boundary being placed at the transition from $\varepsilon = 10^{-6}$ to $10^{-7} \text{ m}^2 \text{ s}^{-3}$.